Tangent fermions: massless fermions on a lattice
Donís Vela, A.

Dynamical simulation of the injection of vortices into a Majorana edge mode

6.1. Introduction

A remarkable property of topological superconductors is that two vortices winding around each other exchange a quasiparticle [36, 88, 100]. This "braiding" operation is a manifestation of the non-Abelian statistics of the Majorana zero-modes bound to the core of an Abrikosov vortex [101–103]. Because Abrikosov vortices are immobile, typically pinned to defects, winding them is a thought experiment that is not easily implemented [104–106].

A proposal to mobilize vortices by injecting them into the edge modes of a topological superconductor was suggested by Beenakker *et al.* [38]. The parity carried by such edge-vortices can be used to encode a qubit. After the injection, the edge-vortices can be braided with bulk vortices due to their chiral motion without requiring any external manipulation. This results in a fermion parity switch (flip of the qubit) between the edges and the bulk that can be detected electrically as an $e/2$ charge pulse when a pair of edge vortices is fused in a normal metal contact [107, 108].

The key component of the braiding device of Ref. 38 is the edge-vortex injector (see Fig. 6.1): it consists of a flux-biased Josephson junction,
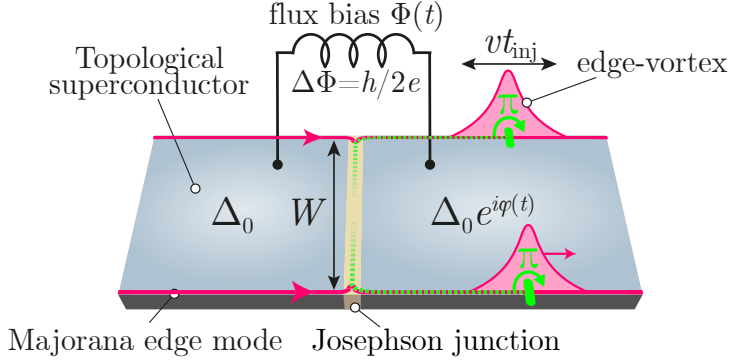
Figure 6.1: Edge vortex injector [38], consisting of a Josephson junction in a topological superconductor with co-propagating chiral edge modes. An $h/2e$ flux increment injects a pair of edge-vortices on opposite edges with a protected fermion parity. The corresponding phase domain wall is represented with green lines. The adiabatic description of the injection process assumes that the injection time $t_{\text{inj}} = (2\pi\xi_{\text{J}}/W)(\text{d}\varphi/\text{d}t)^{-1}$ is long compared to the propagation time W/v along the junction. In this work we relax that assumption, to simulate a device (Fig. 6.2) where these dynamically injected edge-vortices are braided with Abrikosov bulk vortices.

connecting co-propagating chiral edge modes. The application of a flux bias of $h/2e$ increments the superconducting phase φ by 2π. For the fermionic edge mode wave functions this amounts to a π-phase domain wall [37], which moves away from the junction with the Fermi velocity v, carrying the edge-vortex excitations. The injection process takes a finite time t_{inj}, that translates into a finite width vt_{inj} of the domain wall. Given a rate of change $\text{d}\varphi/\text{d}t$, a junction width W, and a superconducting coherence length ξ_{J} one has

$$t_{\text{inj}} = (2\pi\xi_{\text{J}}/W)(\text{d}\varphi/\text{d}t)^{-1}. \tag{6.1}$$

A major simplification of the theoretical description of the injection process arises if t_{inj} is large compared to the propagation time W/v, so for a sufficiently slow rate of change $\text{d}\varphi/\text{d}t \ll 2\pi v\xi_{\text{J}}/W^2$. This is the so-called adiabatic regime, in which one may rely on the instantaneous scattering approximation. Ref. 38 applies to that regime. The purpose of the present work is to relax the adiabatic approximation, to see how large $(v/W)t_{\text{inj}}$ should be for the braiding operation to succeed. This is studied via a fully dynamical simulation of the proposed device during the injection, braiding

and fusion.

Since an edge vortex is a collective degree of freedom, the dynamics involves the full many-body state. We study it numerically, by means of time-dependent Bogoliubov-de Gennes methods. Our main conclusion is that a factor of two between t_{inj} and W/v is sufficient to avoid the excitations of internal degrees of freedom in the junction that would spoil the fermion parity switch [109–112].

The outline of the chapter is as follows: the simulated device and the time-dependent model are introduced in Sec. 6.2. In Sec. 6.3, we present the results of the braiding protocol which recover the main predictions from the adiabatic theory, namely the charge signature at the exit of the device and the fermion parity exchange of the edges with the bulk. Sec. 6.4 describes the excitation dynamics of the junction in the alternative regime $W > vt_{\text{inj}}$ where the braiding protocol cannot hold. The conclusion is presented in Sec. 6.5.

6.2. Model and device

6.2.1. Setup

We consider the device shown in Fig. 6.2 (a). A quantum anomalous Hall (QAH) insulator ($\mathcal{N} = 2$) exhibits an electronic chiral mode (corresponding to two Majorana fermions in the BdG formalism), on each of the two edges [113–115]. When the edge of a QAH is proxitimitized by an s-wave superconductor, the fermionic edge mode splits into two spatialy separated co-propagating chiral Majorana fermions, localized at the edges of the superconducting region [116, 117]. This proximitized system can be described as a topological superconductor ($\mathcal{N} = 1$). In our setup, such a topological superconductor (TSC) with two co-propagating Majorana edge modes (Fig. 6.2 (b)) is divided in three sections by two Josephson junctions, each of length W and thickness w. The junctions are separated by a distance L. Two vortices of flux $\Phi_0 = h/2e$ are created in the bulk by an external magnetic field, one of which is in the region between the two junctions.

A time-dependent flux bias is applied such that the phase in the middle superconductor is $\varphi(t)$ relative to the others, as in Fig. 6.1. By increasing the phase $\varphi(t)$ from 0 to 2π, the effective gap inside the Josephson junctions closes at $\varphi = \pi$ (Fig. 6.2 (c)). In this process, a Josephson vortex [119] passes through each junction, which must locally change the boundary condition from periodic to anti-periodic along the two edges [37] inducing
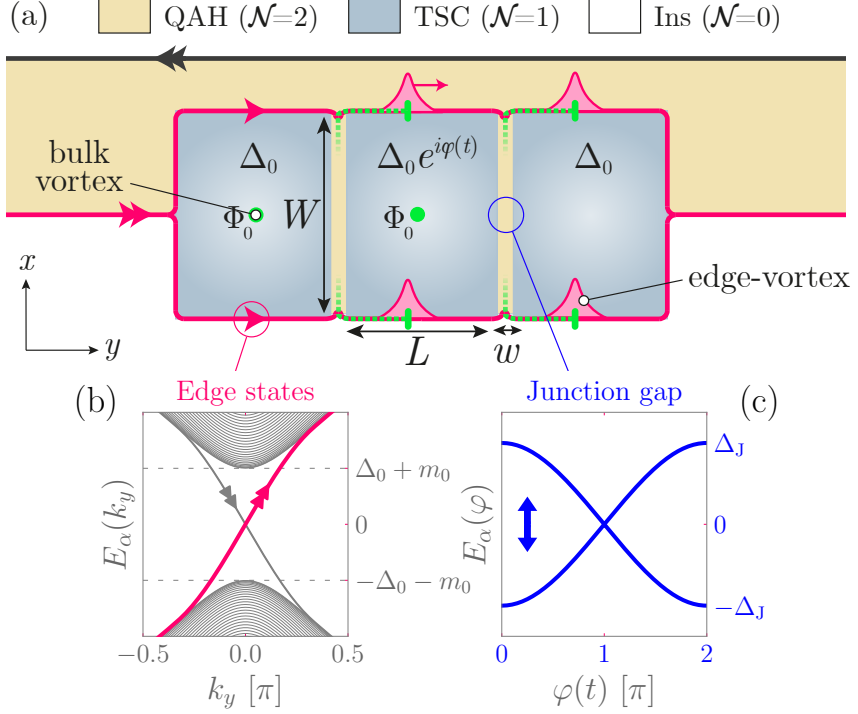
Figure 6.2: (a) Full braiding device: two injectors (as in Fig. 6.1) are used to produce pairs of edge-vortices. The pair of edge-vortices at the back exchanges parity with the bulk vortices upon overtaking a bulk vortex, which is detected by an $e/2$ charge measurement at the exit. (b) Dispersion of Majorana edge modes (magenta), calculated for an infinite strip of a topological superconductor ($\mathcal{N} = 1$). (c) Lowest energy levels in an infinite Josephson junction (described in Sec. 6.2) as a function of the superconducting phase. At $\phi = \pi$ these modes become degenerate and correspond to chiral Majorana edge states propagating along the junction [118].
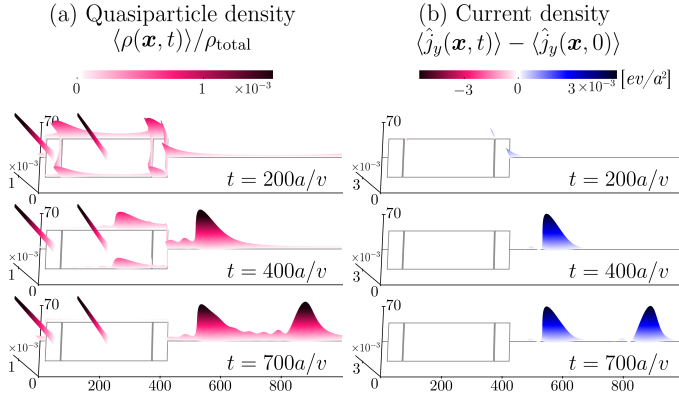
Figure 6.3: Time snapshots of a dynamical simulation of the full device during the injection and braiding protocol, (a) Bogoliubov quasiparticle density as defined in equation (6.19) and (b) current density as defined in (6.11). In this simulation $vt_{\text{inj}} = 1.5W \ll L$, so the edge-vortices injected at the back and front junction are well separated creating two separate $e/2$ charge pulses upon fusion. An animated version can be found at http://link.aps.org/supplemental/10.1103/PhysRevB.108.235309.

a phase domain wall in the wave functions over some characteristic time t_{inj}. This local change of the boundary conditions can be described in terms of an edge vortex field operator $\hat{\mu}(x)$, a collective excitation with non-Abelian statistics [37, 107]. The injected edge-vortices – one pair at the back junction and another pair at the front junction – then propagate along the edges with the Fermi velocity v. The injection time is given by $t_{\text{inj}} = (2\pi\xi_{\text{J}}/W)(\mathrm{d}\varphi(t)/\mathrm{d}t)^{-1}$ where $\xi_{\text{J}} = \hbar v/\Delta_{\text{J}}$ [38] is the coherence length of the junction. Here Δ_{J} denotes the effective gap in the junction [118] (calculated for an infinite junction as shown in Fig. 6.2 (c)). As long as the characteristic injection time is slow compared to W/v, only the two lowest energy states in the finite junction play a role in the dynamics (see App. 6.C).

The edge-vortices of size vt_{inj} then propagate along the edges. The pair of edge-vortices injected at the back overtake a bulk vortex over a distance L. This induces a relative sign flip between the edge vortices and effectively results in a quasiparticle being transferred between the edge vortices and the vortices in the bulk. This parity switch of the edge vortices and the bulk vortices is denoted by $P_{\text{edges}} \to -P_{\text{edges}}$ and $P_{\text{vortices}} \to -P_{\text{vortices}}$, i.e. a flip of the qubit encoded in parity of the edge-vortices.

The braiding event can be detected upon the fusion at the exit of the superconductor via a charge measurement. The edge-vortices injected at the front junction produce a charge $e/2$ independently, while the edge-vortices injected at the back junction produce a charge $\pm e/2$ depending on whether they have braided with the bulk vortex. The resulting net charge at the exit is $e(N_{\text{vortex}} \mod 2)$ with N_{vortex} the number of vortices in between the two injectors. In Fig. 6.3, the local excitation density and local charge during the braiding protocol are shown for an example simulation.

6.2.2. Hamiltonian

The device of Fig. 6.2 is simulated using a tight-binding model of a QAH. In the central regions the QAH is proximitized with an s-wave superconductor. The Hamiltonian is given by [116]:

$$\hat{H}(t) = \frac{1}{2} \sum_{\boldsymbol{x}} \hat{\Psi}^\dagger(\boldsymbol{x}) H(\boldsymbol{k}, \boldsymbol{x}, t) \hat{\Psi}(\boldsymbol{x}) \tag{6.2}$$

where $\hat{\Psi}(\boldsymbol{x}) = (\hat{\psi}_\uparrow(\boldsymbol{x}), \hat{\psi}_\downarrow(\boldsymbol{x}), \hat{\psi}_\downarrow^\dagger(\boldsymbol{x}), -\hat{\psi}_\uparrow^\dagger(\boldsymbol{x}))^\intercal$ is the four component Nambu spinor and H is the Bogoliubov-de-Gennes (BdG) Hamiltonian matrix

$$H(\boldsymbol{k}, \boldsymbol{x}, t) = \begin{pmatrix} H^e(\boldsymbol{k}, \boldsymbol{x}) - \mu & \Delta_0(\boldsymbol{x}) e^{i\vartheta(\boldsymbol{x},t)} \\ \Delta_0(\boldsymbol{x}) e^{-i\vartheta(\boldsymbol{x},t)} & \mu - \mathcal{T} H^e(\boldsymbol{k}, \boldsymbol{x}) \mathcal{T}^{-1} \end{pmatrix} \tag{6.3}$$

with μ the chemical potential and $\mathcal{T} = i\sigma_y \mathcal{K}$ the time-reversal operator (σ_y is the second Pauli matrix in the spin degree of freedom and $\mathcal{K}$ denotes complex conjugation). The electronic block is given by:

$$
\begin{aligned}
H^e(\boldsymbol{k}, \boldsymbol{x}) = {} & \frac{\hbar v}{a} \left(\sigma_x \sin(k_x a) + \sigma_y \sin(k_y a) \right) \\
& + (m_0(\boldsymbol{x}) + M(\boldsymbol{k})) \sigma_z
\end{aligned}
\tag{6.4}
$$

where $M(\boldsymbol{k}) = \frac{2m_1}{a^2} (2 - \cos(k_x a) - \cos(k_y a))$ and $\boldsymbol{k} = -i\nabla$. The simulated system is finite in the x-direction and anti-periodic in the y-direction to ensure that there are no $\boldsymbol{k} = 0$ modes in the edges initially [37, 118].

The different Chern numbers in the regions of Fig. 6.2 are achieved by

different values of m_0 and Δ_0:

$$
\begin{aligned}
m_0(\boldsymbol{x}) &= -0.5, \ \Delta_0(\boldsymbol{x}) = 0: \ \boldsymbol{x} \in \text{QAH} \\
m_0(\boldsymbol{x}) &= -0.5, \ \Delta_0(\boldsymbol{x}) = 1: \ \boldsymbol{x} \in \text{TSC} \\
m_0(\boldsymbol{x}) &= +\infty, \ \ \Delta_0(\boldsymbol{x}) = 0: \ \boldsymbol{x} \in \text{Ins}
\end{aligned}
\tag{6.5}
$$

in units of $\hbar v/a$. The trivial insulating region (Ins) is realized by truncation of the lattice. Furthermore we fix the width of the junction to $w = 2a$ and the length to $W = 42a$. This length ensures that the separation between edges and vortices is much larger than their respective localization lengths. The effective gap Δ_{J} inside the junctions is estimated numerically from the spectrum of an infinitely long junction (see Fig. 6.2), which yields $\Delta_{\text{J}} \approx 0.12\Delta_0$.

In the TSC, $\vartheta(\boldsymbol{x},t) = \eta(\boldsymbol{x}) + \varphi(\boldsymbol{x},t)$ is the pair potential phase with η describing the vortices by $\nabla \times \nabla\eta = \sum_{\boldsymbol{x}_{\text{vortex}}} 2\pi\delta(\boldsymbol{x} - \boldsymbol{x}_{\text{vortex}})$; $\nabla \cdot \nabla\eta = 0$, and $\varphi(\boldsymbol{x},t)$ describing the time-dependent bias, which is only nonzero in the middle superconductor and given by:

$$
\varphi(t) = 2\pi\left(\theta(\tau - t)t/\tau + \theta(t - \tau)\right), \quad t \geq 0
\tag{6.6}
$$

over a characteristic time τ. Here $\theta(t)$ denotes the Heaviside step function. For this profile, the estimated injection time is simply $t_{\text{inj}} = \tau\hbar v/(\Delta_{\text{J}}W)$.

6.2.3. Computation of observables in the evolved many-body state

Before the injection, the system is assumed to be in the stationary ground state of $\hat{H}(0)$ denoted by $|\Omega\rangle$. Here, we consider the evaluation of single-particle operators in the evolved many-body state $\hat{U}(t)|\Omega\rangle$ with the time-evolution operator $\hat{U}(t) = T\exp\left(-(i/\hbar)\int_0^t \hat{H}(t')\mathrm{d}t'\right)$, T being the time-ordering operator. Relative to the initial ground state, the net change in the expectation value of a single-particle operator $\hat{A}$ is denoted:

$$
\langle\hat{A}(t)\rangle - \langle\hat{A}(0)\rangle := \langle\Omega|\hat{U}^\dagger(t)\hat{A}\hat{U}(t)|\Omega\rangle - \langle\Omega|\hat{A}|\Omega\rangle.
\tag{6.7}
$$

The effective description of the superconductor can be reduced to a non-interacting model using the BdG formalism. In App. 6.A.1, we show how we can transform this many-body problem into single-particle problems which can be solved within the first quantization formalism. Eq. (6.7) can

be written as:

$$\langle \hat{A}(t) \rangle - \langle \hat{A}(0) \rangle = \frac{1}{2} \sum_{\alpha \in S^-} \Big(\langle \alpha(t)| A |\alpha(t) \rangle - \langle \alpha| A |\alpha \rangle \Big). \qquad (6.8)$$

Here A is the single-particle BdG operator associated with $\hat{A}$, $|\alpha\rangle := |\alpha(0)\rangle$ denotes the α-th eigenstate of $H(0)$ and $|\alpha(t)\rangle$ obeys

$$i\hbar \partial_t |\alpha(t)\rangle = H(t) |\alpha(t)\rangle. \qquad (6.9)$$

The evolution of the state $|\alpha(t)\rangle$ is calculated numerically using the python package Tkwant [97, 120–123]. This approach has numerical complications as it requires to evolve all the N states in S^- in order to achieve convergence (see App. 6.A.2).

We resolve this issue by writing A in terms of the basis of eigenstates of $H(0)$:

$$\langle \hat{A}(t) \rangle - \langle \hat{A}(0) \rangle = \text{Re} \sum_{\substack{\alpha \in S^- \\ \mu \in S^+}} \sum_{\nu \in S} \langle \alpha(t)|\mu \rangle \langle \mu| A |\nu \rangle \langle \nu|\alpha(t) \rangle. \qquad (6.10)$$

Here the sets S^+ and S^- denote positive and negative energy state indices respectively[1] and S their union $S^+ \cup S^-$. In contrast with Eq. (6.8) (see App. 6.A.2), this form only gives non-zero contributions in a finite range around $E = 0$. This allows us to approximate this expression by truncating the sum and discarding all terms above some energy cut-off, i.e terms with $|E_{\alpha,\mu,\nu}| > E_{\text{max}}$.

6.3. Results

In this section we present the main results of our simulation. We show the charge signature of the braiding protocol and calculate the corresponding parity switch. We consider a system where W is smaller, but comparable to the injection time $vt_{\text{inj}} \approx 2W$. While the theoretical description, relying

---

[1] Notice that particle-hole symmetry enforces that the eigenstates of the BdG Hamiltonian H come in pairs of opposite energies. The eigenspace of zero modes of H must be even dimensional and there must exist a basis of particle-hole partners in it. For each pair, we arbitrarily chose one state to be in S^+ and put its partner in S^-. Thus, in general, S^+ contains zero modes. Overall it contains half of the states (n states) and if we act on them with the particle-hole symmetry operator, we obtain S^-.

on the adiabatic limit, no longer holds for this system we show that the main predictions remain unchanged.

6.3.1. Quantized charge measurement

We first consider the charge signature that can be measured at the exit of the device, after the fusion of the edge vortices. For this we evaluate the current density operator $\hat{j}_y(\boldsymbol{x}) = (ev/a^2)\hat{\Psi}^\dagger(\boldsymbol{x})\nu_0\sigma_y\hat{\Psi}(\boldsymbol{x})$ in the y-direction using Eq. (6.10). Here, ν_0 is the identity acting on the particle-hole degree of freedom. Defining the current as:

$$I(t) = a \sum_{\boldsymbol{x}|y=y_{\text{exit}}} \langle \hat{j}_y(\boldsymbol{x}, t)\rangle - \langle \hat{j}_y(\boldsymbol{x}, 0)\rangle \tag{6.11}$$

the net charge creation is given by the time integral:

$$Q(t) = \int_0^t I(t')\mathrm{d}t'. \tag{6.12}$$

With this, we can calculate the charge pumped during the braiding protocol at the exit of the device (y_{exit}). The spatial separation L between the two Josephson junctions allows to distinguish between two characteristic charge signatures. When $L \gg vt_{\text{inj}}$, the injection events at each junction are well separated in space. In this case, the two pairs of edge-vortices produce separate signals of $\pm\frac{e}{2}$ charge at the exit. The charge contribution of the second pair of edge vortices experiences a sign flip in the presence of bulk vortices, as a consequence of braiding [107]. The theoretical predictions from Refs. 38, 107 are compared with numerical results in the left panel of Fig. 6.4. On the other hand when $L \lesssim vt_{\text{inj}}$, the injection events at both junctions are close, so that the overlapping electrical signals add up, producing a unit charge signature (Fig. 6.4 (b)).

The transferred charge is an indirect probe of the braiding event as it is a result of the fusion between the edge vortices. It is therefore only quantized if the path lengths of the two vortices between injection and fusion are the same [107]. In contrast, the parity exchange is topologically protected, it does not depend on microscopic details. We will check this numerically.

6.3.2. Parity switch of edge-vortices

The phase rotation $\varphi(t) : 0 \to 2\pi$ in the superconductor changes the parity locally carried by the two bulk vortices. Since parity must be
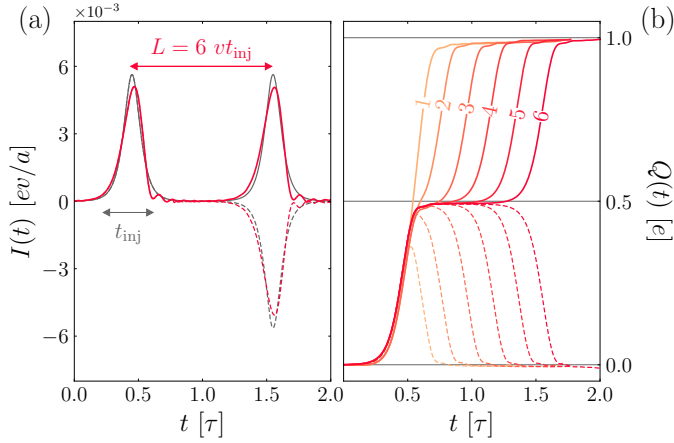
Figure 6.4: (a) Simulated (pink) and theoretical (gray) current density at the exit of the superconductor. A system without (with) vortices is represented with dashed (solid) lines. The pulse width $t_{\mathrm{inj}} \approx \tau/5.17$ is indicated. (b) Corresponding charge increase, for different values of the inter-junction separation L, with values of $L/v\tau$ shown on top of the curves. All simulations have $\tau = 500a/v$ and $W = 42a$.

globally conserved, then necessarily there must be an odd number of excitations elsewhere in the system –namely carried by the edges [38]. This change of parity is a direct consequence of braiding between the bulk and edge vortices. To characterize this process we first identify the parity subsectors that correspond to the states in the bulk vortices and the edges.

The full parity operator can be written –up to the sign of the initial ground state parity– in terms of the Bogoliubov operators as:

$$\hat{P} = \prod_{\alpha \in S^+} \left(1 - 2d_\alpha^\dagger d_\alpha\right). \tag{6.13}$$

We provide a further explanation for this form in App. 6.B.1. In our device, $\hat{P}$ can be split in a product of two terms, the first one corresponding to the bulk vortex excitation (i.e. the fermionic superposition of the two vortex

Majorana zero-modes) and the second one containing all other excitations:

$$\hat{P} = \left(1 - 2d_{\alpha_v}^\dagger d_{\alpha_v}\right) \cdot \prod_{\substack{\alpha \in S^+ \\ \alpha \neq \alpha_v}} \left(1 - 2d_\alpha^\dagger d_\alpha\right)$$

$$:= \hat{P}_{\text{vortices}} \cdot \hat{P}'$$

(6.14)

where α_v is the index of the fermionic state bound to the vortices. This can be done if the vortex state is well isolated from the rest (i.e. there is no hybridization between vortex and edge states). $\hat{P}'$ can be evolved in the Heisenberg picture and expressed in terms of the Bogoliubov operators of the initial Hamiltonian $\{d_\beta\}_{\beta \in S}$. As we show in App. 6.B.1, the time evolution of each d_α can be expanded as

$$\hat{U}^\dagger d_\alpha \hat{U} = \sum_{\beta \in S} \chi_{\alpha\beta} d_\beta \quad \text{with} \quad \chi(t)_{\alpha\beta} = \langle \alpha(0)|\beta(t)\rangle \qquad (6.15)$$

The time evolution of $\hat{P}'$ can then be expressed as a sum of terms of different orders in d operators

$$\hat{U}^\dagger \hat{P}' \hat{U} = \Bigg(1 - 2 \sum_{\alpha \in S^+} \sum_{\mu,\nu \in S} \chi_{\alpha\mu}^* \chi_{\alpha\nu} d_\mu^\dagger d_\nu$$

$$+ 4 \sum_{\substack{\alpha,\beta \in S^+ \\ E_\beta > E_\alpha}} \sum_{\mu,\nu,\sigma,\tau \in S} \chi_{\alpha\mu}^* \chi_{\alpha\nu} \chi_{\beta\sigma}^* \chi_{\beta\tau} d_\mu^\dagger d_\nu d_\sigma^\dagger d_\tau + \cdots \Bigg).$$

(6.16)

Its expectation value in the ground state $|\Omega\rangle$ can then be calculated making use of Wick's theorem up to all orders. The final equation can be found in App. 6.B.1 (Eq. (6.52)).

In our numerical calculation we neglect correlators of order higher than four, and only include states within an energy window E_{max}. This energy window is chosen to match the maximum excitation energy in order for the parity calculation to converge (see App. 6.C).

Since edge and junction states are hybridized, $\hat{P}'$ cannot be decomposed similarly in edge and junction sectors. However, after the bias pump, the expectation value $\langle \hat{P}' \rangle$ can be identified with the parity carried by the edges $\langle \hat{P}_{\text{edge}} \rangle$ as long as the filling of junction states – which only exist for energies $E \geq \Delta_{\text{J}}$ – is negligible. The different intensities of red in Fig. 6.5 show the value obtained for $\hat{P}'$ as we increase E_{max}. We see that convergence is achieved before we need to include any states with energies around Δ_J. This identification of $\langle \hat{P}' \rangle \approx \langle \hat{P}_{\text{edge}} \rangle$ is further supported in
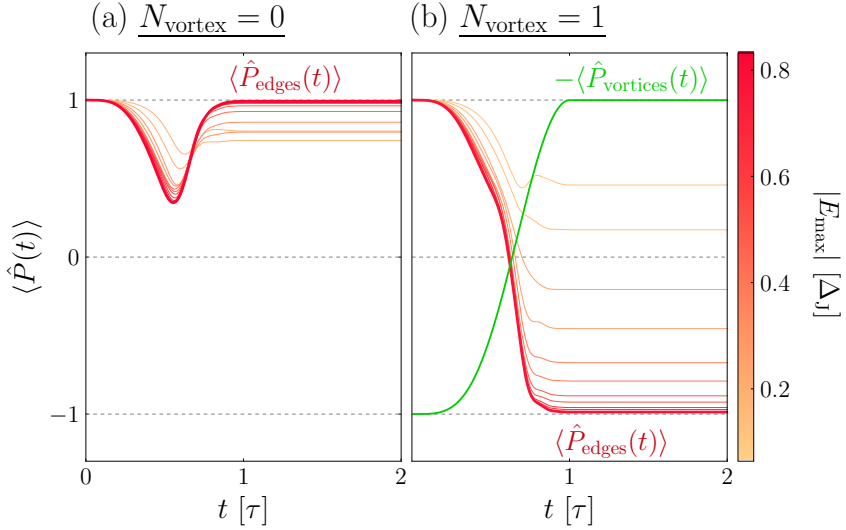
Figure 6.5: Evolution of the parity operator expectation value in the initial ground state without (a) and with vortices (b). In panel (b), the parity of the vortices is separated from the edges, and a parity switch is observed. Convergence of the curves as a function of E_{max} is shown in color.

Sec. 6.4 and App. 6.C.

Fig. 6.5, shows that the parity expectation of the edges is unchanged when there are no vortices, but it switches in the presence of bulk vortices. This demonstrates that, for this set of parametes, the braiding of edge-vortices holds dynamically, and that the internal degrees of freedom in the junction do not spoil the exchange of parity. This implies that neither the adiabatic nor the point junction limits need to be satisfied for braiding to be realised.

6.3.3. Topological protection of the edge vortices

The phase domain wall created during the quench corresponds to a pair of edge vortices that propagate along the edges. As one of them surrounds the bulk vortex it picks up a phase that realises the parity switch [107]. Since a π domain wall cannot be unwound, this mechanism is protected from all local sources of disorder. In this part, we verify that the dynamically injected vortices are topologically protected by introducing irregularities in the spatial profile of $\Delta_0(\boldsymbol{x})$. We show how an additional
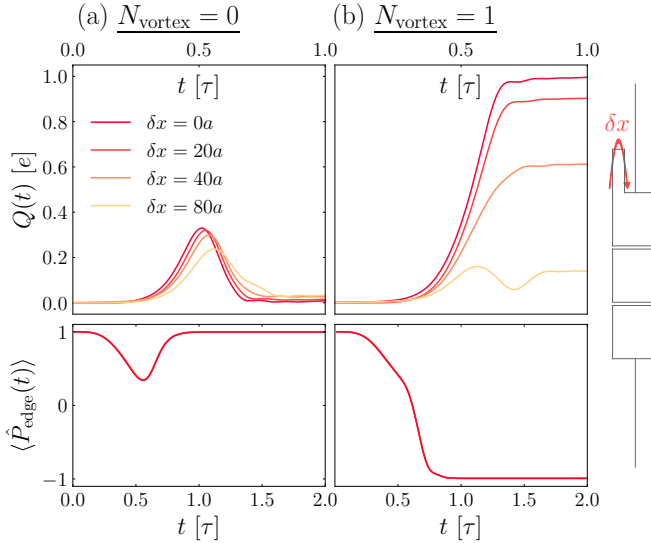
Figure 6.6: (Top) Net charge increase at the exit of the superconductors without (a) and with (b) vortices, with four geometrically induced path length differences between the edges δx for $\tau = 500a/v$. (Bottom) Parity of the edge sector for the same data sets. The calculated parity is independent of δx. In this case the data sets overlap making the different curves indistinguishable.

path-length δx in the upper edge (see the top panel of Fig. 6.6) influences the charge signature, fully spoiling the quantization discussed in Sec. 6.3.1 in agreement with the predictions in Ref. 107. In contrast, our calculation of parity (see the bottom panel of Fig. 6.6) remains unaffected by the local changes in the system, demonstrating the topological protection of the edge-vortex excitations. This confirms that even for a finite junction, edge-vortices can be used to encode protected quantum information.

6.4. Long junction dynamics

Our results so far have considered the particular case $vt_{\mathrm{inj}} \sim 2W$ where the injection process is not spoiled by the excitation of junction modes. In this section, we consider the more general case where the ratio vt_{inj}/W is varied. In particular, we investigate how trapped excitations can influence the creation of edge-vortices for sufficiently long-junctions.

6.4.1. Quasi-particle excitation spectrum

To understand the behaviour in the junction we first study the quasi-particle excitation spectrum $E(\varphi)$. Within the superconducting gap, this spectrum consists of states localized in the bulk vortices, junction and edges. The injection process is characterized by the gap closing at $\varphi = \pi$ with the dispersion $E_J = \pm\Delta_J \cos\varphi/2$ seen before in Fig. 6.2. In our case, the junction states couple with the edge states, forming hybridized bands seen in Fig. 6.7 (gray lines). We calculate the occupation number of these energy levels:

$$\hat{N}(\varphi) = \sum_{E_\mu(\varphi) \in S^+} d_\mu^\dagger(\varphi) d_\mu(\varphi) \qquad (6.17)$$

where each term $d_\mu^\dagger(\varphi) d_\mu(\varphi)$ counts the quasi-particle occupation within a single energy level μ. The expectation value in the evolved state $\hat{U}(t)\,|\Omega\rangle$ is then given by:

$$\langle \hat{N}(\varphi, t) \rangle = \mathrm{Re} \sum_{\substack{\alpha \in S^- \\ \mu \in S^+}} \sum_{\nu \in S} \langle \alpha(t)|\mu^\varphi\rangle \langle \mu^\varphi|\, N\, |\nu^\varphi\rangle \langle \nu^\varphi|\alpha(t)\rangle \qquad (6.18)$$

where $|\mu^\varphi\rangle$ denotes an eigenstate of $H(\varphi)$ and $N = \mathbb{1}$.

The occupation of each level through-out the quench is shown by thick lines in Fig. 6.7, where the color is used to distinguish between edge (red) and junction (blue) states.[2] The slow injection case (a) treated in Sec. 6.3 shows that the junction states are only occupied near values of $\varphi = \pi$ and fully emptied in the edges at the end of the injection. In panel (b), the injection is short enough to create excitations in the levels $E > \Delta_J$. Note that, in this case, the approximation $\langle \hat{P}' \rangle$ made in Sec. 6.3.2 fails because of nonzero occupation in the junction. This means that the parity switch is no longer fully carried by the edge modes, which we attribute to trapped excitations in the Josephson junction.

6.4.2. Trapped excitations

In the presence of a finite Josephson junction the coupling between the two edges is mediated by their hybridization with the chiral states in the Josephson junction. This hybridization is only supported for a duration t_{inj} around $\varphi = \pi$, when the junction is effectively gapless. We have shown that when $vt_{\mathrm{inj}} \sim 2W$ the travel time W/v is short enough to allow the

---

[2]The color at a value φ and band μ is proportional to the value $\sum_{\boldsymbol{x} \in \mathrm{junctions}} |\langle \mu^\varphi|\boldsymbol{x}\rangle|^2$.
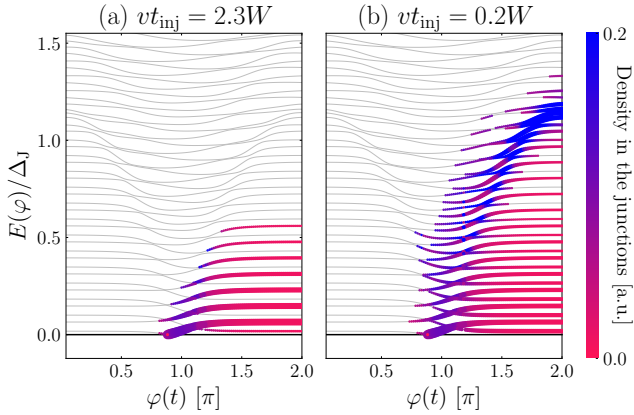
Figure 6.7: Quasi-particle occupation of the energy levels (thick colored lines; a thick line signifies a strong occupation) above the ground state level ($E = 0$), superimposed on the time-independent energy spectrum of $H(\varphi)$ (thin gray lines). The color of the lines distinguishes between junction (blue) and edge (red) states. At fast injection (b), the quasiparticle occupation in the junction levels $E_\mu \geq \Delta_J$ at final time is high. We have removed the vortex state from this figure.

excitations to escape the junctions before the gap re-opens. Here we show that in the alternative regime $vt_{\text{inj}} < W$, the excitation is partially trapped in the gapped bound state of the junction.

In order to describe the quasi-particles inside the junction, we define an excitation density via a spatial projection of the quasi-particle number $N(\boldsymbol{x}) = \mathcal{P}(\boldsymbol{x}) N \mathcal{P}(\boldsymbol{x})$. This is done similarly to our description of charge (i.e. $\langle \boldsymbol{x}' | N(\boldsymbol{x}) | \boldsymbol{x}'' \rangle = \sigma_0 \nu_0 \delta_{\boldsymbol{x}', \boldsymbol{x}''} \delta_{\boldsymbol{x}, \boldsymbol{x}'}$) arriving to the expression:

$$\langle \hat{\rho}_\varphi(x, t) \rangle = \text{Re} \sum_{\substack{\mu \in S^+ \\ \alpha \in S^-}} \sum_{\nu \in S} \langle \alpha(t) | \mu^\varphi \rangle \langle \mu^\varphi | N(\boldsymbol{x}) | \nu^\varphi \rangle \langle \nu^\varphi | \alpha(t) \rangle. \qquad (6.19)$$

Note that when integrated over the whole system, the Eq. (6.18) is recovered. Integrating this density locally gives the number of quasi-particle inside junctions $\langle \hat{N}_{\text{junc}}(t) \rangle$ and edges $\langle \hat{N}_{\text{edges}}(t) \rangle$.

In Fig. 6.8, we show how the quasi-particle changes with time for two different systems. When the injection is slow (a) the quasi-particle number in the junction is fully transferred to the edges as anticipated. In the alternate case when the injection is very fast (b), the particle number slowly
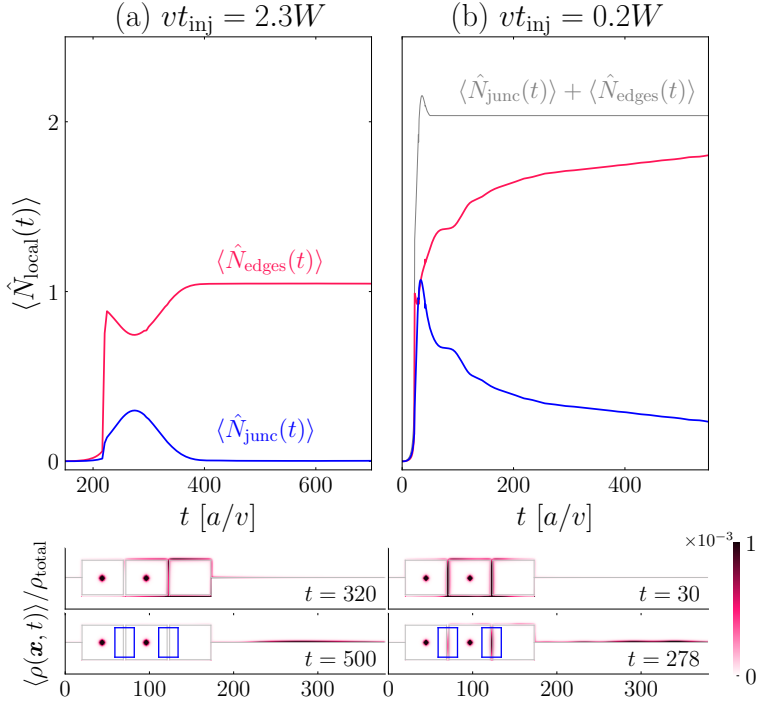
Figure 6.8: Bogoliubov quasi-particle number inside the junction (red) and inside the edges (blue) as a function of time. Panel (a) shows that the junction excitation fully escapes into the edges, while in (b), at short injection time, the junction contains residual quasi-particles. The bottom panels show the corresponding quasi-particle densities at two different times times. The integration window used to calculate the quasi-particle number inside the junction is marked with a blue rectangle. An animated visualisation can be found in http://link.aps.org/supplemental/10.1103/PhysRevB.108.235309.

decays towards a constant residual value in the junctions corresponding to quasi-particles occupying the lowest bound state in the Josephson junctions. As this trapped excitation can carry a part of the parity exchange it can spoil the injection protocol as well as the characteristic charge signature (shown in App. 6.C). For this reason, it is important to find a bound for t_{inj} above which the trapped excitations in the junction can be neglected.

6.4.3. Particle number in the junction

In the adiabatic theory Ref. 38, the total particle number produced in the edges at final time is equal to 1.037. The non-quantized number is due to particle-hole pairs production during the injection process. At slow injection, we find a comparable value $\langle \hat{N}_{junc} \rangle + \langle \hat{N}_{edge} \rangle = 1.049$ as indicated in Fig. 6.8 (a), close to the adiabatic theory. For the fast injection in Fig. 6.8, this is $\langle \hat{N}_{junc} \rangle + \langle \hat{N}_{edge} \rangle = 2.033$ instead.

We therefore turn to a quantitative description of the residual particle number in the junction $\langle \hat{N}_{junc} \rangle$ for different values of vt_{inj}/W. We achieve this by simulating different values of τ in Fig. 6.9. In Fig. 6.9 (a), the particle number is shown as a function of time for different values of vt_{inj}/W, where we distinguish between the two regimes $vt_{inj} > W$ and $vt_{inj} < W$ by two colors. In panel (b), we show that the residual excitation number in the junction decreases fast as the injection time becomes long. We match this with an exponential shown in Fig. 6.9. After $vt_{inj} > 2W$, this value has nearly decayed to zero. In an experimental setting, this provides us with an upper bound on the flux bias change rate $|\mathrm{d}\Phi/\mathrm{d}t| < \Phi_0 v/2W^2\Delta_J$ when the parity exchange is fully carried by the edges corresponding, ensuring a successful injection of edge vortices.

6.5. Conclusion

In this work we have shown how a braiding protocol introduced in Ref. 38 can be dynamically simulated as a tight-binding many-body system. With this setup we were able to fully probe the braiding process away from the limitations of the effective model. This allowed us to investigate the relevant scales in the system as well as compare the current signature with analytical predictions. We were able to study dynamically the local parity switch present in the edge states and show the topological protection of this exchange. We have shown that the injection and braiding of edge-vortices is uncompromised by a finite junction when $vt_{inj} > 2W$, so that all the parity exchange is contained in the edge states. Additionally we studied
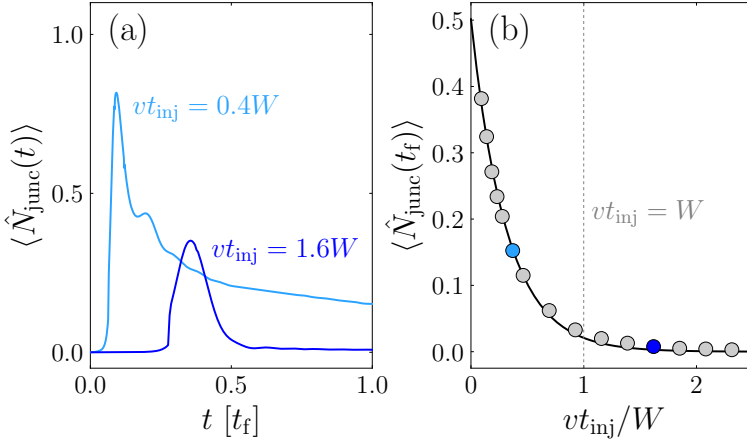
Figure 6.9: (a) Quasi-particle number inside the junction as a function of time, for two values of the injection time. (b) Residual quasi-particle number in the junction at some final time $t_f = 500a/v$ as a function of the ratio vt_{inj}/W. An exponential fit yields $\langle \hat{N}_{\text{junc}}(t_f) \rangle = N_0 \cdot \exp(vt_{\text{inj}}/W\beta)$ with $\beta = 0.31$ and $N_0 = 0.5$.

this system away from this limit and investigated the excitations in the junction. Here, we showed that the lowest bound state of the junction remains excited long after the quench for sufficiently fast injections. While the parity switch $\langle \hat{P}' \rangle$ is still protected in this limit, we can no longer conclude that it is fully carried in the edge states, therefore providing a limitation for the use of such device as a topological qubit. For this reason we show the interplay of scales vt_{inj} and W to find a parameter regime, where the injection of edge vortices is well defined. We see that the adiabatic condition $vt_{\text{inj}} \gg W$ discussed in previous works can be relaxed to $vt_{\text{inj}} \gtrsim W$, while keeping the braiding predictions intact. This is helpful for future experimental work as it allows large deviations from the point junction limit.

6.A. Time-evolution of single-body operators in BdG

6.A.1. From second to first quantization

In a tight-binding system, any single-body operator $\hat{A}$ can be written as

$$\hat{A} = \sum_{\alpha,\beta=1}^{n} A_{\alpha\beta}^{e} \hat{\psi}_{\alpha}^{\dagger} \hat{\psi}_{\beta}, \qquad A_{\alpha\beta}^{e} = \langle 0| \hat{\psi}_{\alpha} \hat{A} \hat{\psi}_{\beta}^{\dagger} |0\rangle, \tag{6.20}$$

where $|0\rangle$ denotes the vacuum of electrons, which can be rewritten into the BdG form as

$$\hat{A} = \frac{1}{2} \hat{\Psi}^{\dagger} A \hat{\Psi} + \frac{1}{2} \operatorname{Tr} A^{e} \tag{6.21}$$

with

$$\begin{aligned} A &= \begin{pmatrix} A^{e} & 0 \\ 0 & -\sigma_{y} A^{e*} \sigma_{y} \end{pmatrix} \\ \hat{\Psi} &:= \begin{pmatrix} \hat{\psi}_{1\uparrow} & \hat{\psi}_{1\downarrow} \cdots & \hat{\psi}_{N/2\uparrow} & \hat{\psi}_{N/2\downarrow} \\ & \hat{\psi}_{1\downarrow}^{\dagger} & -\hat{\psi}_{1\uparrow}^{\dagger} \cdots & \hat{\psi}_{N/2\downarrow}^{\dagger} & -\hat{\psi}_{N/2\uparrow}^{\dagger} \end{pmatrix}^{T} \end{aligned} \tag{6.22}$$

We can evolve this operator in the Heisenberg picture to obtain

$$\hat{U}^{\dagger} \hat{A} \hat{U} = \frac{1}{2} \hat{\Psi}(t)^{\dagger} A \hat{\Psi}(t) + \frac{1}{2} \operatorname{Tr} A^{e} \tag{6.23}$$

where we defined $\hat{\psi}_{\alpha}(t) = \hat{U}^{\dagger} \hat{\psi}_{\alpha} \hat{U}$. Since we intend to evaluate this operator in the ground state $|\Omega\rangle$ of the initial Hamiltonian, we need to write it in terms of the Bogoliubov operators $\{d_{\beta}\}_{\nu \in S}$ of $\hat{H}(0)$. It is possible to prove (see App. 6.A.3) that the $\{\hat{\psi}_{\alpha}(t)\}_{\nu \in S}$ operators can be written as linear combinations of these Bogoliubov operators as

$$\hat{\psi}_{\alpha}(t) = \sum_{\beta \in S} \Phi_{\alpha\beta}(t) d_{\beta} \qquad \text{i.e.} \qquad \hat{\Psi}(t) = \Phi(t)\mathbf{d} \tag{6.24}$$

where $\Phi(0)$ is the matrix that diagonalises the BdG Hamiltonian at $t = 0$, (i.e. $H(0) = \Phi(0)\mathcal{E}\Phi^{\dagger}(0)$) and $\Phi(t)$ is the solution of

$$i\hbar\partial_{t}\Phi(t) = H(t)\Phi(t). \tag{6.25}$$

Notice that this means that the columns of Φ are none other than the eigenstates of $H(0)$ evolved according to the Schrödinger equation for $H(t)$. With this, we can express

$$\hat{U}^\dagger \hat{A} \hat{U} = \frac{1}{2} \mathbf{d}^\dagger \Phi^\dagger A \Phi \mathbf{d} + \frac{1}{2} \operatorname{Tr} A^e \tag{6.26}$$

Finally, using the fact that by definition $\langle \Omega | d_\alpha^\dagger d_\beta | \Omega \rangle = \delta_{\alpha\beta}$ if $E_\alpha < 0$ and $\langle \Omega | d_\alpha^\dagger d_\beta | \Omega \rangle = 0$ otherwise, we obtain

$$\langle \hat{A}(t) \rangle - \langle \hat{A}(0) \rangle = \frac{1}{2} \sum_{\alpha \in S^-} \left(\Phi^\dagger(t) A \Phi(t) - \Phi^\dagger(0) A \Phi(0) \right)_{\alpha\alpha}, \tag{6.27}$$

which in Dirac notation becomes

$$\langle \hat{A}(t) \rangle - \langle \hat{A}(0) \rangle = \frac{1}{2} \sum_{\alpha \in S^-} \left(\langle \alpha(t)| A |\alpha(t)\rangle - \langle \alpha(0)| A |\alpha(0)\rangle \right). \tag{6.28}$$

With this, we have mapped our original problem of evolving many-body states in a Hilbert space of dimension 2^n into n first quantization problems in a Hilbert space of dimension $2n$.

6.A.2.   Convergence

The fact that Eq. (6.28) involves all n negative energy eigenstates of H poses two problems. First, we only aim at describing the system accurately at low energies. Any realistic system will not share the specific high-energy behaviour of our tight-binding description far from the Fermi energy. Secondly, we should be able to understand our system by considering only states close to the Fermi energy, so evolving all of them is a waste of computational resources. Unfortunately we have no reason to belive that the contribution of both terms in Eq. (6.28) will cancel out as we go away from the Fermi energy. This was actually studied numerically and it was verified that the value of $\langle \hat{\jmath}_y(\boldsymbol{x}, t) \rangle - \langle \hat{\jmath}_y(\boldsymbol{x}, 0) \rangle$ as given by Eq. (6.28) does not converge –instead it oscillates– as we increase the amount of states evolved (see Fig. 6.10). This section is devoted to rewrite this equation in a form that solves this issue. To do so, let us explicitly make use of basis of the eigenstates of $H(0)$ and introduce the completeness relation around

A in the first term of Eq. (6.28) to obtain

$$
\frac{1}{2} \sum_{\alpha \in S^-} \langle \alpha(t) | A | \alpha(t) \rangle =
$$

$$
\frac{1}{2} \sum_{\alpha \in S^-} \sum_{\mu,\nu \in S} \langle \alpha(t) | \mu \rangle \langle \mu | A | \nu \rangle \langle \nu | \alpha(t) \rangle =
$$

$$
\frac{1}{2} \sum_{\alpha \in S^-} \sum_{\mu,\nu \in S^-} \Big(\langle \alpha(t) | \mu \rangle \langle \mu | A | \nu \rangle \langle \nu | \alpha(t) \rangle \tag{6.29}
$$
$$
+ \langle \alpha(t) | \mathcal{C}\mu \rangle \langle \mathcal{C}\mu | A | \nu \rangle \langle \nu | \alpha(t) \rangle
$$
$$
+ \langle \alpha(t) | \mu \rangle \langle \mu | A | \mathcal{C}\nu \rangle \langle \mathcal{C}\nu | \alpha(t) \rangle
$$
$$
+ \langle \alpha(t) | \mathcal{C}\mu \rangle \langle \mathcal{C}\mu | A | \mathcal{C}\nu \rangle \langle \mathcal{C}\nu | \alpha(t) \rangle \Big).
$$

where $\mathcal{C} = \sigma_y \nu_y \mathcal{K}$ is the BdG charge conjugation operator and $\mathcal{C}\mu$ denotes the particle-hole partner of the state labeled μ. Since $\hat{A}$ is a single-particle operator, it satisfies $\mathcal{C}A\mathcal{C} = -A$. Given that $\{|\alpha(t)\rangle : \alpha \in (S^- \cup S^+)\}$ is a complete basis of the BdG Hilbert space, we can write the first term of Eq. (6.29) as

$$
\frac{1}{2} \sum_{\alpha \in S^-} \sum_{\mu,\nu \in S^-} \langle \alpha(t) | \mu \rangle \langle \mu | A | \nu \rangle \langle \nu | \alpha(t) \rangle =
$$

$$
\frac{1}{2} \sum_{\mu \in S^-} \langle \mu | A | \mu \rangle \tag{6.30}
$$

$$
- \frac{1}{2} \sum_{\alpha \in S^+} \sum_{\mu,\nu \in S^-} \langle \mathcal{C}\alpha(t) | \mu \rangle \langle \mu | A | \nu \rangle \langle \nu | \mathcal{C}\alpha(t) \rangle
$$

If we plug this in Eq. (6.29) and then in Eq. (6.28), a few simplifications happen. The first term of this equation will cancel with the second term of Eq. (6.28), and the second term of Eq. (6.30) is real and equal to the last term of Eq. (6.29) (this follows from the properties of $\mathcal{C}$). In addition, the second and third terms of Eq. (6.29) are each other's complex conjugate. Taking all of this into account we can write down Eq. (6.28) as

$$
\langle \hat{A}(t) \rangle - \langle \hat{A}(0) \rangle =
$$
$$
\mathrm{Re} \sum_{\alpha \in S^-} \sum_{\mu,\nu \in S^+} \Big(\langle \alpha(t) | \mu \rangle \langle \mu | A | \nu \rangle \langle \nu | \alpha(t) \rangle \tag{6.31}
$$
$$
+ \langle \alpha(t) | \mu \rangle \langle \mu | A | \mathcal{C}\nu \rangle \langle \mathcal{C}\nu | \alpha(t) \rangle \Big)
$$
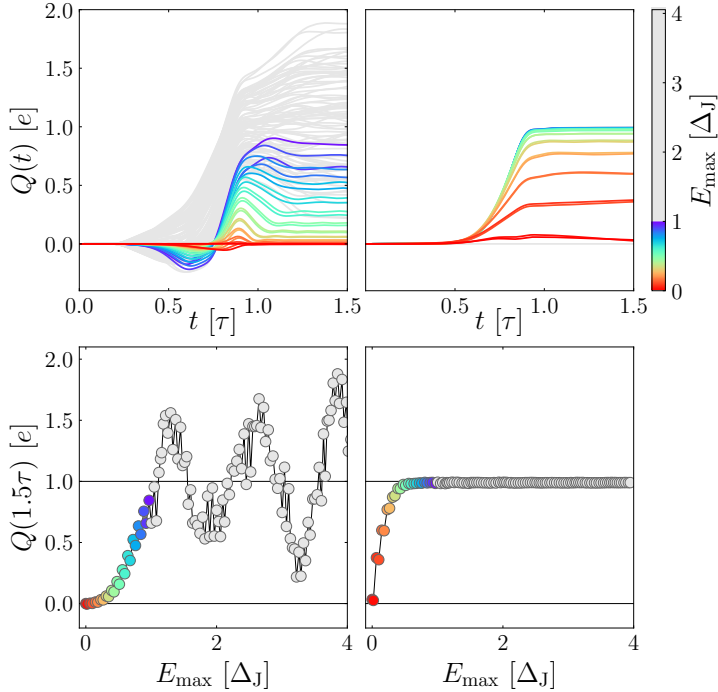
Figure 6.10: Convergence of the charge at the exit with two methods. Left: with charge expressed in the local basis using Eq. (6.27) where $E_{\max}$ is the maximum energy of the states in the sum over α. Right: With charge expressed in the basis of eigenstates of $H(0)$ using Eq. (6.32) where $E_{\max}$ is the maximum energy of the states in the sums over α, μ and ν.

which we write more simply in the main text as

$$\langle \hat{A}(t) \rangle - \langle \hat{A}(0) \rangle = \mathrm{Re} \sum_{\substack{\alpha \in S^- \\ \mu \in S^+}} \sum_{\nu \in S} \langle \alpha(t)|\mu \rangle \langle \mu| A |\nu \rangle \langle \nu|\alpha(t) \rangle \qquad (6.32)$$

This formula includes overlaps between positive energy and evolved negative energy states which ensures non-zero contributions to only exist around $E = 0$. In Fig. 6.10 we show how the contribution of the terms in the sum vanishes as we go further away from the Fermi energy, which lets us avoid having to evolve all negative energy states.

6.A.3.   Proof of time evolution method

In this section we prove the following statement:

Proposition. *Let $\hat{\Psi}$ be the Nambu spinor of fermion creation and annihilation operators as defined in Eq. (6.22) satisfying $\{\hat{\psi}_\alpha, \hat{\psi}_\beta^\dagger\} = \delta_{\alpha,\beta}$ and $\{\hat{\psi}_\alpha, \hat{\psi}_\beta\} = \delta_{\alpha,\mathcal{C}\beta}$ where $\mathcal{C}\alpha$ is the index of $(\hat{\psi}_\alpha)^\dagger$ in $\hat{\Psi}$ (i.e. $\hat{\psi}_{\mathcal{C}\alpha} = \hat{\psi}_\alpha^\dagger$).*
Let

$$\hat{H}(t) = \frac{1}{2}\hat{\Psi}^\dagger H(t) \hat{\Psi}$$

be the time-dependent BdG Hamiltonian describing a tight-binding superconducting system of fermions. Let $\hat{U}(t)$ be its corresponding evolution operator. Let $\mathcal{C}$ be the antiunitary charge conjugation operator satisfying $\mathcal{C}^2 = 1$ and $\{\mathcal{C}, H\} = 0$. Let $V(t)$ be a matrix that diagonalises $H(t)$ and let $\mathbf{d} = (d_1, d_2, \cdots, d_{2n})$ be the spinor of Bogoliubov operators diagonalising $\hat{H}(0)$.

Then, the time evolution of $\hat{\Psi}$ can we written as

$$\hat{\Psi}(t) := \hat{U}(t)^\dagger \hat{\Psi}\hat{U}(t) = \Phi(t)\mathbf{d} \tag{6.33}$$

where Φ obeys

$$i\hbar\partial_t\Phi(t) = H(t)\Phi(t), \qquad \Phi(0) = V(0) \tag{6.34}$$

Proof. According to Heisenberg's picture evolution equation we have

$$i\partial_t\hat{\psi}_\alpha(t) = \left[\hat{\psi}_\alpha(t), \hat{U}(t)^\dagger\hat{H}(t)\hat{U}(t)\right]. \tag{6.35}$$

Since $\hat{H}$ is quadratic in $\hat{\Psi}$, we know that $\hat{\psi}_\alpha(t)$ can be expanded in terms of the initial $\hat{\psi}$'s as

$$\hat{\psi}_\alpha(t) = \sum_\beta \zeta_{\alpha\beta}(t)\hat{\psi}_\beta, \tag{6.36}$$

or in matrix notation

$$\hat{\Psi}(t) = \zeta(t)\hat{\Psi}. \tag{6.37}$$

Notice that the unitarity of $\hat{U}$ imposes that the operators in $\hat{\Psi}(t)$ satisfy the same commutation algebra as the initial ones. In turn, this imposes unitarity on ζ. We can use Eq. (6.36) to write the commutator in Eq. (6.35) as

$$\left[\hat{\psi}_\kappa(t), \hat{U}(t)^\dagger\hat{H}(t)\hat{U}(t)\right] = \frac{1}{2}\sum_{\alpha\beta\mu\nu\lambda} H_{\alpha\beta}\zeta_{\alpha\mu}^*\zeta_{\beta\nu}\zeta_{\kappa\lambda}[\hat{\psi}_\lambda, \hat{\psi}_\mu^\dagger\hat{\psi}_\nu] \tag{6.38}$$

It is easy to check that

$$[\hat{\psi}_\lambda, \hat{\psi}_\mu^\dagger \hat{\psi}_\nu] = \hat{\psi}_\nu \delta_{\lambda,\mu} - \hat{\psi}_\mu^\dagger \delta_{\lambda,\mathcal{C}\nu}, \tag{6.39}$$

so we get

$$\begin{aligned}
\left[\hat{\psi}_\kappa(t), \hat{U}(t)^\dagger \hat{H}(t)\hat{U}(t)\right] &= \frac{1}{2}\sum_{\alpha\beta\mu\nu} H_{\alpha\beta}\zeta_{\alpha\mu}^*\zeta_{\beta\nu}\zeta_{\kappa\mu}\hat{\psi}_\nu \\
&- \frac{1}{2}\sum_{\alpha\beta\mu\nu} H_{\alpha\beta}\zeta_{\alpha\mu}^*\zeta_{\beta\nu}\zeta_{\kappa\mathcal{C}\nu}\hat{\psi}_\mu^\dagger.
\end{aligned} \tag{6.40}$$

Using $\hat{\psi}_\mu^\dagger = \hat{\psi}_{\mathcal{C}\mu}$ and relabeling in the last term we can rewrite

$$\begin{aligned}
&\left[\hat{\psi}_\kappa(t), \hat{U}(t)^\dagger \hat{H}(t)\hat{U}(t)\right] = \\
&\frac{1}{2}\sum_{\alpha\beta\mu\nu} H_{\alpha\beta}\zeta_{\alpha\mu}^*\zeta_{\beta\nu}\zeta_{\kappa\mu}\hat{\psi}_\nu - \frac{1}{2}\sum_{\alpha\beta\mu\nu} H_{\alpha\beta}\zeta_{\alpha\mu}^*\zeta_{\beta\nu}\zeta_{\kappa,\mathcal{C}\nu}\hat{\psi}_{\mathcal{C}\mu} = \\
&\frac{1}{2}\sum_{\alpha\beta\mu\nu} H_{\alpha\beta}\zeta_{\alpha\mu}^*\zeta_{\beta\nu}\zeta_{\kappa\mu}\hat{\psi}_\nu - \frac{1}{2}\sum_{\alpha\beta\mu\nu} H_{\alpha\beta}\zeta_{\alpha,\mathcal{C}\nu}^*\zeta_{\beta,\mathcal{C}\mu}\zeta_{\kappa\mu}\hat{\psi}_\nu.
\end{aligned} \tag{6.41}$$

Comparing with the left-hand side of Eq. (6.35) we can deduce that

$$i\partial_t \zeta_{\kappa\nu} = \frac{1}{2}\sum_{\alpha\beta\mu} H_{\alpha\beta}\zeta_{\alpha\mu}^*\zeta_{\beta\nu}\zeta_{\kappa\mu} - \frac{1}{2}\sum_{\alpha\beta\mu} H_{\alpha\beta}\zeta_{\alpha,\mathcal{C}\nu}^*\zeta_{\beta,\mathcal{C}\mu}\zeta_{\kappa\mu} \tag{6.42}$$

From $\hat{\psi}_\alpha^\dagger(t) = \psi_{\mathcal{C}\alpha}(t)$, we have $\zeta_{\alpha\beta} = \zeta_{\mathcal{C}\alpha,\mathcal{C}\beta}^*$ so the previous equation becomes

$$i\partial_t \zeta_{\kappa\nu} = \frac{1}{2}\sum_{\alpha\beta\mu} H_{\alpha\beta}\zeta_{\alpha\mu}^*\zeta_{\beta\nu}\zeta_{\kappa\mu} - \frac{1}{2}\sum_{\alpha\beta\mu} H_{\alpha\beta}\zeta_{\mathcal{C}\alpha,\nu}\zeta_{\mathcal{C}\beta,\mu}^*\zeta_{\kappa\mu} \tag{6.43}$$

The particle-hole symmetry of H ($\mathcal{C}H\mathcal{C} = -H$) can be expressed element-wise as $H_{\mathcal{C}\alpha,\mathcal{C}\beta} = -H_{\beta,\alpha}$. After some relabeling on the last term, this lets us rewrite the previous equation as

$$i\partial_t \zeta_{\kappa\nu} = \sum_{\alpha\beta\mu} H_{\alpha\beta}\zeta_{\alpha\mu}^*\zeta_{\beta\nu}\zeta_{\kappa\mu} \tag{6.44}$$

The unitarity of ζ implies $\sum_\mu \zeta_{\alpha\mu}^*\zeta_{\kappa\mu} = \delta_{\alpha\kappa}$ so the previous expression

becomes

$$i\partial_t \zeta_{\alpha\beta} = \sum_\mu H_{\alpha\mu}\zeta_{\mu\beta} \tag{6.45}$$

or in matrix notation

$$i\partial_t \zeta = H\zeta, \qquad \zeta(0) = \mathbb{1} \tag{6.46}$$

Now notice that we can compose Eq. (6.36) with $\hat{\Psi} = V(0)\mathbf{d}$ and define $\Phi(t) = \zeta(t)V(0)$ that satisfies Eq. (6.33). Since $V(0)$ is time-independent, Eq. (6.34) follows immediately from Eq. (6.46). $\qquad\qquad\square$

6.B. Parity

6.B.1. Time evolution of the parity operator

The parity operator is defined as:

$$\hat{P} = (-1)^{\sum_{\alpha=1}^n \hat{\psi}_\alpha^\dagger \hat{\psi}_\alpha} = \prod_{\alpha=1}^n \left(1 - 2\hat{\psi}_\alpha^\dagger \hat{\psi}_\alpha\right). \tag{6.47}$$

Since it commutes with $\hat{H}$, its ground state is an eigenstate of parity. This, together with the fact that the BdG operators switch the parity of a state, implies that we can also write down our parity operator in terms of them:

$$\hat{P} = p_\Omega \prod_{\alpha \in S^+}^n \left(1 - 2d_\alpha^\dagger d_\alpha\right) \tag{6.48}$$

where $p_\Omega = \pm 1$ stands for the parity of the ground state. In general, we can express the parity of a set of quasi-particle states S as

$$\hat{P}_S = \prod_{\alpha \in S} \left(1 - 2d_\alpha^\dagger d_\alpha\right) \tag{6.49}$$

The time evolution of this operator is given by substituting each d_α for $d_\alpha(t) = \hat{U}^\dagger d_\alpha \hat{U}$. From the results of App. 6.A.1, it is straightforward to obtain the expression of $d_\alpha(t)$ in terms of $\{d_\alpha\}_{\alpha \in S}$:

$$\hat{U}^\dagger \mathbf{d}\hat{U} = \hat{U}^\dagger V(0)^\dagger \hat{\Psi}\hat{U} = V(0)^\dagger \hat{\Psi}(t) = V(0)^\dagger \Phi(t)\mathbf{d} \tag{6.50}$$

Thus, if we define $\chi(t) = V(0)^\dagger \hat{\Psi}(t)$ we have

$$\hat{U}^\dagger d_\alpha \hat{U} = \sum_{\beta \in S} \chi(t)_{\alpha\beta} d_\beta \qquad \chi(t)_{\alpha\beta} = \langle \alpha | \beta(t) \rangle \qquad (6.51)$$

We can expand the product in Eq. (6.49) and use Wick's theorem to obtain an expression for the time evolution of $\langle \hat{P}_S \rangle$

$$\langle \hat{P}_S(t) \rangle = \sum_{m=0}^{n_S} (-2)^m \sum_{\substack{0 < \alpha_1 \\ < \ldots < \alpha_m}} \sum_{c \in C_m} (-1)^{s(c)} \prod_{k=1}^{m} \Theta_{\alpha_{i_k(c)}\alpha_{j_k(c)}}^{X_k(c)Y_k(c)}. \qquad (6.52)$$

This formula contains several elements. First, we have a sum over all orders $0 < m < n_S$ (the term corresponding to $m = 0$ is equal to 1). For each order m we sum over all unordered choices of m states among n_S. For every such choice, we sum over all possible Wick contractions of that order (C_m denotes the set of all Wick contractions of order m). For some order m, each contraction (c denotes a specific contraction) in this sum results in a specific product of m numbers of the form $\Theta_{\alpha\beta}^{XY}$ defined as

$$\Theta_{\alpha\beta}^{00} = \sum_{\mu \in S^-} \chi_{\alpha,\mu}^* \chi_{\beta,\mu}$$

$$\Theta_{\alpha\beta}^{01} = \sum_{\mu \in S^-} \chi_{\alpha,\mu}^* \chi_{\beta,\mathcal{C}\mu}^*$$

$$\Theta_{\alpha\beta}^{10} = \sum_{\mu \in S^-} \chi_{\alpha,\mathcal{C}\mu} \chi_{\beta,\mu} = \Theta_{\beta\alpha}^{01*} \qquad (6.53)$$

$$\Theta_{\alpha\beta}^{11} = \sum_{\mu \in S^-} \chi_{\alpha,\mathcal{C}\mu} \chi_{\beta,\mathcal{C}\mu}^* = \delta_{\alpha\beta} - \Theta_{\alpha\beta}^{00*}$$

Each contraction c of order m corresponds to a permutation of the numbers $\{1, 2, \cdots, 2m\}$ under the following restriction: when the elements of the permutation are split in pairs $\{(a_k(c), b_k(c))\}_{k=1}^m$ they must satisfy $a_k(c) < b_k(c) \in \{1, \ldots, 2m\}$ and $a_1(c) < a_2(c) < \cdots < a_m(c)$. Each pair yields $i_k(c) = \lfloor (a_k(c)+1)/2 \rfloor$, $j_k(c) = \lfloor (b_k(c)+1)/2 \rfloor$, $X_k(c) = (a_k(c)+1) \mod 2$ and $Y_k(c) = b_k(c) \mod 2$. The overall sign $s(c)$ is the sign of the permutation. It is possible to write a script that procedurally generates all valid permutations and calculates the indices $X_k(c)$, $Y_k(c)$, $\alpha_{i_k(c)}$ and $\alpha_{j_k(c)}$ corresponding to every contraction c.

6.B.2.   Convergence of parity

The amount of terms in equation Eq. (6.52) is

$$1 + \sum_{m=1}^{n_S} \binom{n_S}{m}(2m-1)!!. \tag{6.54}$$

This number is out of reach in practice, so we are forced to truncate the sums. It was checked that restricting ourselves to order $m_{\max} = 4$ is sufficient to get an accurate result. In addition, the operator $\langle P' \rangle$ defined in 6.14 in principle contains $n_S = n - 1$ Bogoliubov operators, but in practice we must truncate the product to a maximum number of states $n_{\max}$, or equivalently, a cut-off energy $E_{\max}$. In Sec. 6.3.2, we have argued that it is necessary to keep $E_{\max} < \Delta_{\rm J}$ so that $\langle \hat{P}' \rangle$ represents the parity of the edges. This is true for the case where $vt_{\rm inj}/W = 2.3$ studied in Sec. 6.3. We show this explicitly in Fig. 6.11, where convergence is reached approximately at $0.85\Delta_{\rm J}$, ensuring that no junction states participate in the calculation of the parity. We also show a few other cases with smaller values of $vt_{\rm inj}/W$. For these values, convergence of parity requires including up to 35 states with energies above $\Delta_{\rm J}$. In this case the calculation includes the hybridized edge and bound states of the junction, which does not allow us to isolate the edge parity sector from the junction.

6.C.   Supplemental results

In this section, we present the results of our simulation for variable quenching times, supplementing the results in the main text.

6.C.1.   Local representation of observables

The calculations of current and quasi-particle number made in the main text have been integrated over specific areas. Here we show a few snapshots of the local current density and the local excitation density for two values of $vt_{\rm inj}/W$ (left and right panels of Fig. 6.12). We show three different times in which the injection and fusion can be observed.

In the left panels, for long injections, the excitation entirely leaves the junction. In the right panel (which corresponds with Fig. 6.8), the excitation density slowly decays from the junction, at times even after $t > \tau = 50a/v$ when the quench is over.
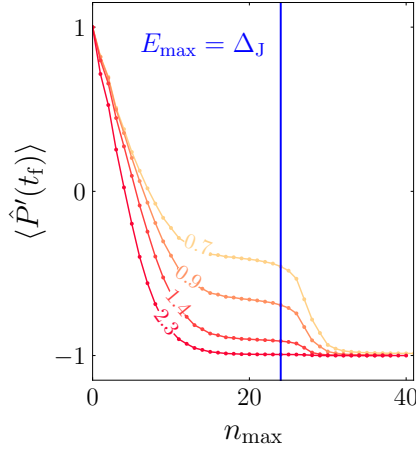
Figure 6.11: Convergence of the parity sector $\hat{P}'$ at final time t_{f} as a function of the index n_{max} which counts the number of eigenstates included in the calculation. This is done for different values of vt_{inj}/W which are displayed on the curves. For energies above $E_{\mathrm{max}} = \Delta_{\mathrm{J}}$, the hybridized edge-junction states are necessary in the convergence of the operator.

The current density is zero in the superconducting region as the Majorana fermions are chargeless. Only upon fusion, the excitations produce charge. Here, the charge production at short injection times is much smaller, which is shown quantitatively in the next part. It is worth noting that while the excitations can remain trapped in the junction, they do not carry charge.

6.C.2. Current density in the long junction regime

For completeness, we include the calculations of charge at the exit for the different quenching times. In Fig. 6.13 we show the excitation spectrum, quasi-particle number, current and charge for different values of vt_{inj}/W discussed in Sec. 6.4. We can see how the the occupancy of the junction increases when the injection time becomes shorter.

As the contribution of the excitations in the junction became sufficient the predictions for quantized charge are no longer valid. This can be seen in the bottom part of Fig. 6.13 charge is no longer quantized. In the cases $vt_{\mathrm{inj}}/W = 0.1, 0.2$, not only the lowest mode but also the next higher mode of the junction is populated by excitations. Additionally as shown in Fig. 6.12, a fast injection causes a large path-length difference as the
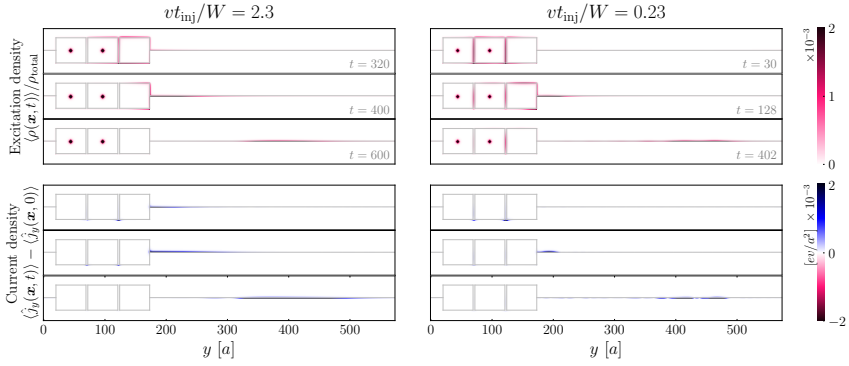
Figure 6.12: Three snapshots of the braiding protocol for two values of vt_{inj}/W (left column and right column). the top panel shows the snapshots in terms of the local excitation density, and the bottom panel shows them in terms of the local current density.

junction traps the excitations and leaks them into the top and bottom edges at different rates. This results in further interference effects upon fusion.
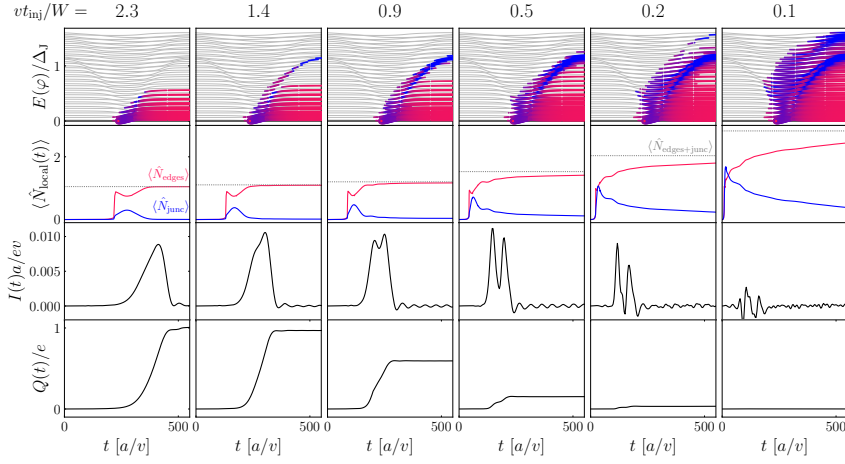
Figure 6.13: First row: Quasi-particle occupation of the energy levels (thick colored lines). The color of the lines distinguishes between junction (blue) and edge (red) states. Second row: Quasi-particle number in the junction (blue), edges (red) and their sum at final value (gray dashed line). Third row: Current at the exit of the superconductor. Fourth row: Net charge creation at the exit of the superconductor.

Bibliography

[1] P. R. WALLACE. The band theory of graphite. *Phys. Rev.*, **71**, 622–634 (1947).

[2] K. S. NOVOSELOV, A. K. GEIM, S. V. MOROZOV, D. JIANG, M. I. KATSNELSON, I. V. GRIGORIEVA, S. V. DUBONOS & A. A. FIRSOV. Two-dimensional gas of massless Dirac fermions in graphene. *Nature*, **438**, 197–200 (2005).

[3] H. NIELSEN & M. NINOMIYA. A no-go theorem for regularizing chiral fermions. *Phys. Lett. B*, **105**, 219–223 (1981).

[4] D. B. KAPLAN. A method for simulating chiral fermions on the lattice. *Physics Letters B*, **288**, 342–347 (1992).

[5] Y. SHAMIR. Chiral fermions from lattice boundaries. *Nuclear Physics B*, **406**, 90–106 (1993).

[6] H. NEUBERGER. Exactly massless quarks on the lattice. *Physics Letters B*, **417**, 141–144 (1998).

[7] H. NEUBERGER. More about exactly massless quarks on the lattice. *Physics Letters B*, **427**, 353–355 (1998).

[8] R. STACEY. Eliminating lattice fermion doubling. *Phys. Rev. D*, **26**, 468–472 (1982).

[9] C. Le, Z. Yang, F. Cui, A. P. Schnyder & C.-K. Chiu. Generalized fermion doubling theorems: Classification of two-dimensional nodal systems in terms of wallpaper groups. *Phys. Rev. B*, **106**, 045126 (2022).

[10] H. Tasaki. Physics and mathematics of quantum many-body systems. *Springer* (2020).

[11] K. G. Wilson. Confinement of quarks. *Phys. Rev. D*, **10**, 2445–2459 (1974).

[12] L. Susskind. Lattice fermions. *Phys. Rev. D*, **16**, 3031–3039 (1977).

[13] S. D. Drell, M. Weinstein & S. Yankielowicz. Strong-coupling field theories. II. fermions and gauge fields on a lattice. *Phys. Rev. D*, **14**, 1627–1647 (1976).

[14] P. H. Ginsparg & K. G. Wilson. A remnant of chiral symmetry on the lattice. *Phys. Rev. D*, **25**, 2649–2657 (1982).

[15] S. Hong, V. Diep, S. Datta & Y. P. Chen. Modeling potentiometric measurements in topological insulators including parallel channels. *Phys. Rev. B*, **86**, 085131 (2012).

[16] K. M. M. Habib, R. N. Sajjad & A. W. Ghosh. Chiral tunneling of topological states: Towards the efficient generation of spin current using spin-momentum locking. *Phys. Rev. Lett.*, **114**, 176801 (2015).

[17] B. Messias de Resende, F. C. de Lima, R. H. Miwa, E. Vernek & G. J. Ferreira. Confinement and fermion doubling problem in dirac-like hamiltonians. *Phys. Rev. B*, **96**, 161113 (2017).

[18] A. L. Araújo, R. P. Maciel, R. G. F. Dornelas, D. Varjas & G. J. Ferreira. Interplay between boundary conditions and wilson's mass in dirac-like hamiltonians. *Phys. Rev. B*, **100**, 205111 (2019).

[19] J. Kogut & L. Susskind. Hamiltonian formulation of Wilson's lattice gauge theories. *Phys. Rev. D*, **11**, 395–408 (1975).

[20] J. P. Costella. A new proposal for the fermion doubling problem, arXiv:hep-lat/0207008 (2002).

[21] Z.-X. Li, A. Vaezi, C. B. Mendl & H. Yao. Numerical observation of emergent spacetime supersymmetry at quantum criticality. *Science Adv.*, **4**, eaau1463 (2018).

[22] T. C. Lang & A. M. Läuchli. Quantum Monte Carlo simulation of the chiral Heisenberg Gross-Neveu-Yukawa phase transition with a single Dirac cone. *Phys. Rev. Lett.*, **123**, 137602 (2019).

[23] Y. Da Liao, X. Y. Xu, Z. Y. Meng & Y. Qi. Caution on Gross-Neveu criticality with a single Dirac cone: Violation of locality and its consequence of unexpected finite-temperature transition. *Phys. Rev. B*, **108**, 195112 (2023).

[24] Z. Wang, F. Assaad & M. Ulybyshev. Validity of slac fermions for the (1+1)-dimensional helical luttinger liquid. *Phys. Rev. B*, **108**, 045105 (2023).

[25] C. M. Bender, K. A. Milton & D. H. Sharp. Consistent formulation of fermions on a Minkowski lattice. *Phys. Rev. Lett.*, **51**, 1815–1818 (1983).

[26] M. J. Pacholski, G. Lemut, J. Tworzydło & C. W. J. Beenakker. Generalized eigenproblem without fermion doubling for Dirac fermions on a lattice. *SciPost Phys.*, **11**, 105 (2021).

[27] L. Fu & C. L. Kane. Superconducting proximity effect and Majorana Fermions at the surface of a topological insulator. *Phys. Rev. Lett.*, **100**, 096407 (2008).

[28] C. Kallin & J. Berlinsky. Chiral superconductors. *Rep. Prog. Phys.*, **79**, 054502 (2016).

[29] Z. Zhu, M. Papaj, X.-A. Nie, H.-K. Xu, Y.-S. Gu, X. Yang et al. Discovery of segmented Fermi surface induced by Cooper pair momentum. *Science*, **374**, 1381–1385 (2021).

[30] G. E. Volovik. Quantum phase transitions from topology in momentum space. *Lect. Notes Phys.*, **718**, 31–73 (2007).

[31] C. W. J. Beenakker. Bogoliubov Fermi surface revealed. *J. C. Cond. Matt. Phys.* (2020).

[32] S. Rao. Introduction to non-abelian anyons. *arXiv:1610.09260* (2016).

[33] A. Kitaev. Fault-tolerant quantum computation by anyons. *Ann. Phys.*, **303**, 2–30 (2003).

[34] N. READ & G. MOORE. Fractional Quantum Hall Effect and Nonabelian Statistics. *Prog. Theor. Phys. Supp.*, **107**, 157–166 (1992).

[35] R. L. WILLETT, C. NAYAK, K. SHTENGEL, L. N. PFEIFFER & K. W. WEST. Magnetic-field-tuned Aharonov-Bohm oscillations and evidence for non-abelian anyons at $\nu = 5/2$. *Phys. Rev. Lett.*, **111**, 186401 (2013).

[36] C. W. J. BEENAKKER. Search for non-Abelian Majorana braiding statistics in superconductors. *SciPost Phys. Lect. Notes*, page 15 (2020).

[37] P. FENDLEY, M. P. A. FISHER & C. NAYAK. Edge states and tunneling of non-Abelian quasiparticles in the $\nu = 5/2$ quantum Hall state and $p + ip$ superconductors. *Phys. Rev. B*, **75**, 045317 (2007).

[38] C. W. J. BEENAKKER, P. BAIREUTHER, Y. HERASYMENKO, I. ADAGIDELI, L. WANG & A. R. AKHMEROV. Deterministic creation and braiding of chiral edge vortices. *Phys. Rev. Lett.*, **122**, 146803 (2019).

[39] M. Z. HASAN & C. L. KANE. Topological insulators. *Rev. Mod. Phys.*, **82**, 3045–3067 (2010).

[40] X.-L. QI & S.-C. ZHANG. Topological insulators and superconductors. *Rev. Mod. Phys.*, **83**, 1057–1110 (2011).

[41] C. L. KANE. Topological band theory and the $\mathbb{Z}_2$ invariant. *Contemporary Concepts of Condensed Matter Science*, **6**, 3–34 (2013).

[42] J. W. BRAUN, Q. SU & R. GROBE. Numerical approach to solve the time-dependent Dirac equation. *Phys. Rev. A*, **59**, 604–612 (1999).

[43] P. KREKORA, Q. SU & R. GROBE. Klein paradox in spatial and temporal resolution. *Phys. Rev. Lett.*, **92**, 040406 (2004).

[44] G. R. MOCKEN & C. H. KEITEL. FFT-split-operator code for solving the Dirac equation in 2+1 dimensions. *Comp. Phys. Comm.*, **178**, 868–882 (2008).

[45] F. FILLION-GOURDEAU, E. LORIN & A. D. BANDRAUK. Numerical solution of the time-dependent Dirac equation in coordinate space without fermion-doubling. *Comp. Phys. Comm.*, **183**, 1403–1415 (2012).

[46] J. TWORZYDŁO, C. W. GROTH & C. W. J. BEENAKKER. Finite difference method for transport properties of massless Dirac fermions. *Phys. Rev. B*, **78**, 235438 (2008).

[47] M. SUZUKI. Fractal decomposition of exponential operators with applications to many-body theories and Monte Carlo simulations. *Phys. Lett. A*, **146**, 319–323 (1990).

[48] N. WATANABE & M. TSUKADA. Fast and stable method for simulating quantum electron dynamics. *Phys. Rev. E*, **62**, 2914–2923 (2000).

[49] A. CHAVES, L. COVACI, K. Y. RAKHIMOV, G. A. FARIAS & F. M. PEETERS. Wave-packet dynamics and valley filter in strained graphene. *Phys. Rev. B*, **82**, 205430 (2010).

[50] K. MOCHIZUKI, T. BESSHO, M. SATO & H. OBUSE. Topological quantum walk with discrete time-glide symmetry. *Phys. Rev. B*, **102**, 035418 (2020).

[51] S. RYU, A. P. SCHNYDER, A. FURUSAKI & A. W. W. LUDWIG. Topological insulators and superconductors: tenfold way and dimensional hierarchy. *New J. Phys*, **12**, 065010 (2010).

[52] C. ROIESNEL. Definition of the covariant lattice Dirac operator. *Phys. Rev. D*, **87**, 074505 (2013).

[53] A. D. VELA, G. LEMUT, M. J. PACHOLSKI, J. TWORZYDŁO & C. W. J. BEENAKKER. Reflectionless Klein tunneling of Dirac fermions: Comparison of split-operator and staggered-lattice discretization of the Dirac equation. *J. Phys. Cond. Matt.*, **34**, 364003 (2022).

[54] A. GEORGE. Nested dissection of a regular finite element mesh. *SIAM J. Numer. Anal.*, **10**, 345–363 (1973).

[55] A. GEORGE & E. NG. On the complexity of sparse *QR* and *LU* factorization of finite-element matrices. *SIAM J. Sci. Stat. Comput.*, **9**, 849–861 (1988).

[56] X. S. LI & J. W. DEMMEL. SuperLU_DIST: A scalable distributed-memory sparse direct solver for unsymmetric linear systems. *ACM Trans. Math. Softw.*, **29**, 110–140 (2003).

[57] P. E. ALLAIN & J. N. FUCHS. Klein tunneling in graphene: optics with massless electrons. *Eur. Phys. J. B*, **83**, 301 (2011).

[58] C. W. J. BEENAKKER. Andreev reflection and Klein tunneling in graphene. *Rev. Mod. Phys.*, **80**, 1337–1354 (2008).

[59] O. VAFEK & A. VISHWANATH. Dirac fermions in solids: From high-T_c cuprates and graphene to topological insulators and Weyl semimetals. *Ann. Rev. Cond. Matt. Phys.*, **5**, 83–112 (2014).

[60] T. KIMURA. Domain-wall, overlap, and topological insulators, arXiv:1511.08286 (2015).

[61] R. HAMMER, W. PÖTZ & A. ARNOLD. Single-cone real-space finite difference scheme for the time-dependent Dirac equation. *J. Comp. Phys.*, **265**, 50–70 (2014).

[62] W. PÖTZ. Single-cone finite-difference schemes for the (2+1)-dimensional Dirac equation in general electromagnetic textures. *Phys. Rev. E*, **96**, 053312 (2017).

[63] A. DONÍS VELA, M. J. PACHOLSKI, G. LEMUT, J. TWORZYDŁO & C. W. J. BEENAKKER. Massless Dirac fermions on a space-time lattice with a topologically protected Dirac cone. *Ann. Phys. (Berl.)*, **534**, 2200206 (2022).

[64] R. HAMMER & W. PÖTZ. Dynamics of domain-wall Dirac fermions on a topological insulator: A chiral fermion beam splitter. *Phys. Rev. B*, **88**, 235119 (2013).

[65] W. PÖTZ & R. HAMMER. Chiral fermion dynamics in 2d magnetic vortices: Manifestation of momentum-spin-locking. *J. Appl. Phys.*, **120**, 193903 (2016).

[66] W. PÖTZ & M. SCHREILECHNER. Single-cone finite difference scheme for the (2+1)D Dirac von Neumann equation. *J. Comp. Phys.*, **348**, 591–611 (2017).

[67] W. PÖTZ. Perfectly matched layers for the Dirac equation in general electromagnetic texture. *Phys. Rev. E*, **103**, 013301 (2021).

[68] R. HAMMER & W. PÖTZ. Staggered grid leap-frog scheme for the (2+1)D Dirac equation. *Comp. Phys. Comm.*, **185**, 40–52 (2014).

[69] R. STACEY. Gauge invariance and fermion doubling on the lattice. *Z. Phys. C*, **19**, 75–78 (1983).

[70] C. J. GRIFFIN & T. D. KIEU. Fermion doubling and gauge invariance on random lattices. *Phys. Rev. Lett.*, **70**, 3844–3847 (1993).

[71] D. TONG. Lattice gauge theory, lecture notes at https://www.damtp.cam.ac.uk/user/tong/gaugetheory.html (2018).

[72] B. A. BERNEVIG & T. L. HUGHES. Topological Insulators and Topological Superconductors. *Princeton* (2013).

[73] I. I. RABI. Das freie Elektron im homogenen Magnetfeld nach der Diracschen Theorie. *Z. Physik*, **49**, 507–511 (1928).

[74] J. W. McCLURE. Diamagnetism of graphite. *Phys. Rev.*, **104**, 666–671 (1956).

[75] P. CHENG, C. SONG, T. ZHANG, Y. ZHANG, Y. WANG, J.-F. JIA ET AL. Landau quantization of topological surface states in Bi_2Se_3. *Phys. Rev. Lett.*, **105**, 076801 (2010).

[76] T. HANAGURI, K. IGARASHI, M. KAWAMURA, H. TAKAGI & T. SASAGAWA. Momentum-resolved Landau-level spectroscopy of Dirac surface state in Bi_2Se_3. *Phys. Rev. B*, **82**, 081305 (2010).

[77] Y. JIANG, Y. WANG, M. CHEN, Z. LI, C. SONG, K. HE, L. WANG, X. CHEN, X. MA & Q.-K. XUE. Landau quantization and the thickness limit of topological insulator thin films of Sb_2Te_3. *Phys. Rev. Lett.*, **108**, 016401 (2012).

[78] S. K. CHONG, R. TSUCHIKAWA, J. HARMER, T. D. SPARKS & V. V. DESHPANDE. Landau levels of topologically-protected surface states probed by dual-gated quantum capacitance. *ACS Nano*, **14**, 1158–1165 (2020).

[79] A. J. M. GIESBERS, U. ZEITLER, M. I. KATSNELSON, L. A. PONOMARENKO, T. M. MOHIUDDIN & J. C. MAAN. Quantum-Hall activation gaps in graphene. *Phys. Rev. Lett.*, **99**, 206803 (2007).

[80] C.-K. CHIU, J. C. Y. TEO, A. P. SCHNYDER & S. RYU. Classification of topological quantum matter with symmetries. *Rev. Mod. Phys.*, **88**, 035005 (2016).

[81] Y. AHARONOV & A. CASHER. Ground state of a spin-1/2 charged particle in a two-dimensional magnetic field. *Phys. Rev. A*, **19**, 2461–2462 (1979).

[82] L. ALVAREZ-GAUMÉ. Supersymmetry and the Atiyah-Singer index theorem. *Comm. Math. Phys.*, **90**, 161–173 (1983).

[83] M. I. KATSNELSON. Graphene — Carbon in two dimensions. *Cambridge* (2012).

[84] F. BRUCKMANN, G. ENDRŐDI, M. GIORDANO, S. D. KATZ, T. G. KOVÁCS, F. PITTLER & J. WELLNHOFER. Landau levels in QCD. *Phys. Rev. D*, **96**, 074506 (2017).

[85] G. S. BALI, B. B. BRANDT, G. ENDRŐDI & B. GLÄSSLE. Meson masses in electromagnetic fields with Wilson fermions. *Phys. Rev. D*, **97**, 034505 (2018).

[86] C. W. J. BEENAKKER & L. KOUWENHOVEN. A road to reality with topological superconductors. *Nature Phys.*, **12**, 618–621 (2016).

[87] M. SATO & Y. ANDO. Topological superconductors: a review. *Rep. Prog. Phys.*, **80**, 076501 (2017).

[88] N. READ & D. GREEN. Paired states of fermions in two dimensions with breaking of parity and time-reversal symmetries and the fractional quantum Hall effect. *Phys. Rev. B*, **61**, 10267–10297 (2000).

[89] A. P. MACKENZIE, T. SCAFFIDI, C. W. HICKS & Y. MAENO. Even odder after twenty-three years: the superconducting order parameter puzzle of Sr_2RuO_4. *npj Quantum Materials*, **2**, 40 (2017).

[90] M. KAYYALHA, D. XIAO, R. ZHANG, J. SHIN, J. JIANG, F. WANG ET AL. Absence of evidence for chiral Majorana modes in quantum anomalous Hall-superconductor devices. *Science*, **367**, 64–67 (2020).

[91] M. TINKHAM. Introduction to Superconductivity. *Dover Publications* (2004).

[92] N. F. Q. YUAN & L. FU. Zeeman-induced gapless superconductivity with a partial Fermi surface. *Phys. Rev. B*, **97**, 115139 (2018).

[93] M. PAPAJ & L. FU. Creating Majorana modes from segmented Fermi surface. *Nature Comm.*, **12**, 577 (2021).